

# Crater mound formation by wind erosion on Mars

Liam Steele<sup>1</sup>, Edwin Kite<sup>1</sup> and Timothy Michaels<sup>2</sup>

1. Department of Geophysical Sciences, University of Chicago, Chicago, Illinois, USA  
(liamsteele@uchicago.edu).
2. SETI Institute, Mountain View, California, USA.

## Abstract

Most of Mars’ ancient sedimentary rocks by volume are in wind-eroded sedimentary mounds, but the connections between mound form and wind erosion are unclear. We perform mesoscale simulations of different crater and mound morphologies to understand the formation of sedimentary mounds. As crater depth increases, slope winds produce increased erosion near the base of the crater wall, forming mounds. Peak erosion rates occur when the crater depth is  $\sim 2$  km. Mound evolution depends on the size of the host crater. In smaller craters mounds preferentially erode at the top, becoming more squat, while in larger craters mounds become steeper-sided. This agrees with observations where smaller craters tend to have proportionally shorter mounds, and larger craters have mounds encircled by moats. If a large-scale sedimentary layer blankets a crater, then as the layer recedes across the crater it will erode more towards the edges of the crater, resulting in a crescent-shaped moat. When a 160 km diameter mound-hosting crater is subject to a prevailing wind, the surface wind stress is stronger on the leeward side than on the windward side. This results in the center of the mound appearing to ‘march upwind’ over time, and forming a ‘bat-wing’ shape, as is observed for Mt. Sharp in Gale crater.

## 1 Introduction

Landscape evolution on Earth is a competition between tectonics and rainfall (e.g. Burbank and Anderson, 2011). On Mars, both these factors have been negligible for at least 3 Gyr, allowing slow landscape evolution through aeolian processes to dominate. Thus, Mars is a natural laboratory for exploring the co-evolution of wind and landscapes (e.g. Holt et al., 2010; Conway et al., 2012; Brothers et al., 2013; Brothers and Holt, 2016). In this study, we focus on layered sediments in craters. Most of these sediments are indurated (Malin and Edgett, 2000), and we refer to them as sedimentary rocks.

Most of the known light-toned, post-Noachian sedimentary rocks on Mars take the form of mountains (mounds) within craters and canyons (Hynek et al., 2003), including Mt. Sharp in Gale crater, the target of the Mars Science Laboratory ‘Curiosity’ rover (Anderson and Bell, 2010; Milliken et al., 2010). The other currently operating Mars rover, MER-B ‘Opportunity’, is also exploring a crater that contains a sedimentary mound; the 22 km diameter Endeavour crater (e.g. Squyres et al., 2012; Grant et al., 2016). These mounds are distributed across the Martian surface, with most of the mapped intra-crater mounds located in the Arabia

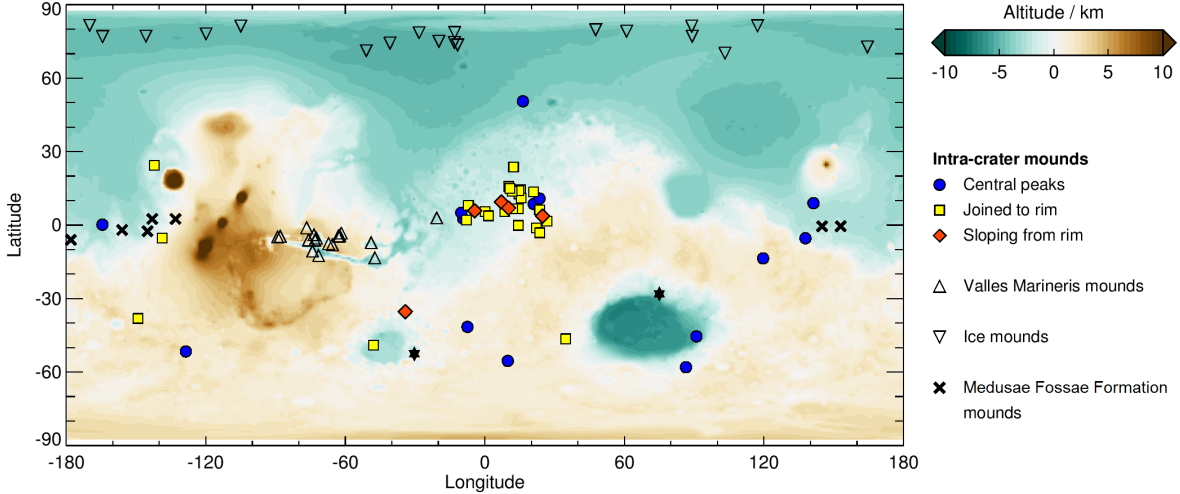


Figure 1: Global distribution of mapped sedimentary mounds on shaded MOLA topography, showing intra-crater mounds (Bennett and Bell, 2016), Valles Marineris mounds (Kite et al., 2016), ice mounds (Conway et al., 2012) and Medusae Fossae Formation mounds (Bradley et al., 2002). The two black stars show mounds in the Terby and Galle craters that were mapped but not included in Kite et al. (2016).

Terra region (Malin and Edgett, 2000; Ferguson and Christensen, 2008; Zabrusky et al., 2012; Bennett and Bell, 2016). Figure 1 shows the locations of intra-crater mounds (the focus of this study), as well as mounds within the Valles Marineris canyon system (Kite et al., 2016), ice mounds in the north polar region (Conway et al., 2012) and Medusa Fossae Formation mounds (Bradley et al., 2002). Visually, the intra-crater mounds mapped by Bennett and Bell (2016) fall into three main types. There are mounds with a distinctive moat encircling them, mounds joined partly to the crater wall, and mounds forming a ramp down from the crater rim (see Figure 2). The data suggest that there is a tendency for mounds completely encircled by moats (Figure 2e,f) to become more frequent as the crater diameter increases, while mounds defined here as ramps (Figure 2a,b) occur only in craters  $< 60$  km in diameter (see Figure 3).

Despite the central role of mounds in the sedimentary-rock landscapes of Mars, the mechanisms responsible for mound formation and evolution remain unclear. One hypothesis for the presence of mounds is that they are the result of wind erosion of initially sediment-filled craters, with material preferentially eroded around the edges of the craters (Malin and Edgett, 2000; Andrews-Hanna et al., 2010; Bennett and Bell, 2016). Wind tunnel experiments carried out by Day et al. (2016) show that a mound and moat can be shaped by wind erosion, though these experiments used damp sand as opposed to sedimentary rock, with a crater model 30 cm in diameter. Large eddy simulations (Day et al., 2016; Anderson and Day, 2017) suggest that vortical flows emanating from the upwind crater rim are responsible for moat excavation in sediment-filled craters, with a positive-feedback mechanism in which the erosion

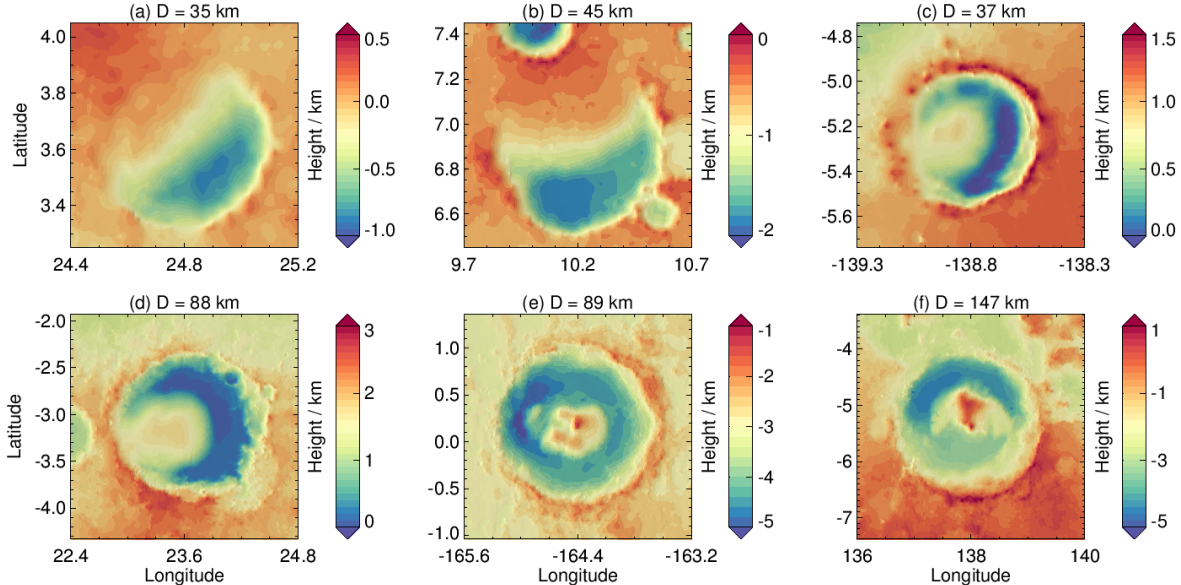


Figure 2: Mars Orbiter Laser Altimeter (MOLA) elevation data of intra-crater mounds (as listed in Bennett and Bell, 2016) showing a variety of mound morphologies, with (a,b) mounds forming a ramp down from the rim, (c,d) mounds joined to the crater wall, and (e,f) mounds encircled by moats. Craters are unnamed apart from (e) Nicholson and (f) Gale. Crater diameters are listed above each panel.

potential of the sediment increases the more the sediment erodes. Chan and Netoff (2017) present a wind-sculpted sandstone mound on Earth as an analogue to Gale crater, though it is  $O(10^3)$  times smaller. Another hypothesis, motivated by outward dips in sedimentary mound strata, is that some mounds form in place by interspersed episodes of aeolian deposition and slope-wind erosion (Kite et al., 2013, 2016). In either hypothesis, winds play a vital role in the erosion of sedimentary deposits, and the transport of sediment within or away from the crater.

Wind erosion occurs on Mars today, as evidenced by dune field activity (e.g. Fenton, 2006; Silvestro et al., 2010, 2013; Chojnacki et al., 2011). Observations of dune field morphologies and other aeolian features can be used to infer present-day and potential paleowind directions (e.g. Hobbs et al., 2010; Bridges et al., 2014; Day and Kocurek, 2016). Estimated sedimentary-rock erosion rates are between  $0.01\text{--}50 \mu\text{m yr}^{-1}$ , with the higher rates corresponding to vertical rock faces (e.g. Bridges et al., 2012; Farley et al., 2014; Golombek et al., 2014; Grindrod and Warner, 2014; Levy et al., 2016; Salese et al., 2016; Kite and Mayer, 2017). Rates  $>1 \mu\text{m yr}^{-1}$  allows for many kilometers of cumulative erosion (Armstrong and Leovy, 2005). Some of the strongest winds within craters are slope winds on crater walls (e.g. Kite et al., 2013; Tyler and Barnes, 2013, 2015; Rafkin et al., 2016; Newman et al., 2017; Steele et al., 2017). Due to the low density of the Martian atmosphere, the heating and cooling of the surface has a much larger impact on the near-surface atmosphere than on Earth. Due to the correspondingly

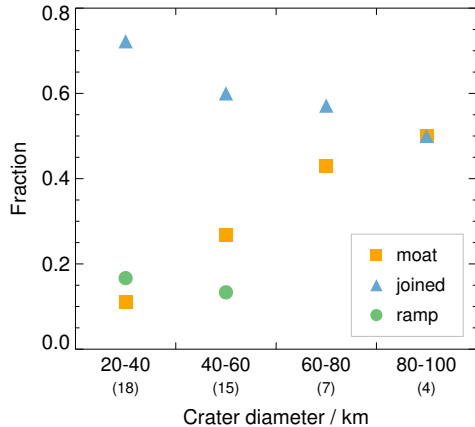


Figure 3: The fraction of craters from Bennett and Bell (2016) in each size bin that have mounds displaying the characteristics of mounds encircled by moats, mounds joined to the rim or mounds forming a ramp down from the rim (see Figure 2 for mound types). The numbers in brackets under each size range show how many craters are in that bin. The Becquerel mound is ambiguous and is excluded.

strong horizontal temperature gradients, the resulting slope winds are typically 2–3 times faster than on Earth (e.g. Ye et al., 1990; Savijarvi and Siili, 1993; Tyler et al., 2002; Spiga and Forget, 2009; Spiga, 2011). Indeed, the strong nighttime downslope winds can increase near-surface air temperatures by up to 20 K (Spiga et al., 2011).

Several processes may contribute to slope-wind erosion; (i) rock weakening and break-up by weathering and/or hydration state changes (e.g. Chipera and Vaniman, 2007; Wang et al., 2011); (ii) mass wasting, followed by aeolian removal of talus to maintain steep slopes and allow continued mass wasting; (iii) aeolian erosion of weakly cemented sediments (Shao, 2008); and (iv) aeolian abrasion of bedrock (Wang et al., 2011). These processes range from transport-limited to detachment-limited, and predict correspondingly different shear-stress dependencies and thresholds for erosion. However, what they all have in common is the need for wind. Thus, in order to identify physical mechanisms involved in sedimentary mound formation and evolution, we need to obtain an understanding of the diurnal variation of slope winds, and the feedback between terrain evolution and circulation. To achieve this, we use a mesoscale model to simulate the circulation within craters of different morphologies. We assume detachment-limited erosion, where only the magnitude of the wind is of concern (as opposed to transport-limited erosion, where wind vectors are required for determining the transport of the eroded sediment). This is complementary to the large eddy simulations of Day et al. (2016) and Anderson and Day (2017), where the focus was on vortical flows and not the radial slope winds.

## 2 Model description

Simulations are performed using the three-dimensional non-hydrostatic Mars Regional Atmospheric Modeling System (MRAMS) mesoscale model (Rafkin et al., 2001). This model has been used extensively to investigate many features of the Martian circulation (e.g. Michaels, 2006; Michaels et al., 2006; Michaels and Rafkin, 2008; Pla-Garcia et al., 2016; Rafkin et al., 2002; Rafkin and Michaels, 2003; Rafkin, 2009; Rafkin et al., 2016).

Two types of simulation were performed: ‘idealized’ and ‘realistic’. The purpose of the idealized simulations is to isolate only those circulations related to crater topography. As such, the simulations have the Coriolis force and thermal tides removed, and are initialized without large-scale winds. This is similar to the approach used by Tyler and Barnes (2015). Three nested grids are used, with the resolution of the innermost grid ranging between 0.5–4 km, depending on the size of the crater being simulated (80 grid boxes span the crater diameter). There are 60 vertical levels, with the midpoint of the lowest level at 15 m above the surface, and with 15 levels in the lowest kilometer. Tests were performed with increased numbers of vertical levels, but there were no significant changes in the strengths of the slope flows. Time steps in the outermost grid vary between 2–8 s, depending on the crater diameter, and are reduced by a factor of two for each successive grid. The surrounding topography has constant albedo (0.23), thermal inertia ( $230 \text{ J m}^{-2} \text{ K}^{-1} \text{ s}^{-1/2}$ ) and aerodynamic surface roughness (3 cm). For computational simplicity the transport of individual dust particles is not modeled here, and instead the visible dust optical depth at 610 Pa is set to a constant value of 0.45. The water cycle is not included. Craters are located at  $0^\circ\text{N}$ ,  $0^\circ\text{E}$ , at  $L_S = 135^\circ$ , resulting in sunrise and sunset times of 05:30 and 17:30 respectively. Different times of year were tested, but the results changed little.

For the ‘realistic’ simulations we use five nested grids, with the size of the outer grid,  $O(10^4 \text{ km})$ , chosen so that the crater circulations that develop on the inner grids are not directly affected by the boundary conditions. The grid spacings of the outer and inner grids are 324 km and 4 km respectively (decreasing by a factor of three with each successive grid). A time step of 8 s is used in the outer grid, and this is decreased by a factor of two for each successive grid. Surface properties are interpolated from TES nighttime thermal inertia and albedo data sets (Putzig and Mellon, 2007), with the topography from MOLA 32 pixel per degree (ppd) data (Smith et al., 2001). Output from the LMD global circulation model (e.g. Forget et al., 1999) is used to provide the initial conditions and boundary conditions every 1.5 Mars hours at four different times of year:  $L_S = 45^\circ$ ,  $135^\circ$ ,  $225^\circ$  and  $315^\circ$ . For both the ‘idealized’ and ‘realistic’ cases, simulations are performed for 7 sols, with model data output every 20 Mars minutes. The last sol is used for analysis, in order to give the model time to ‘spin up’, though the atmospheric temperatures and circulations patterns are repeatable after around 3–4 sols.

In this study we assume that saltation abrasion is the landscape-modifying mechanism, and that physical or chemical weathering processes break down the sediment, producing grains suitable for saltation. As such, we use the surface wind stress distributions from the simulations as a proxy for erosion. The surface wind stress is given by  $\tau_* = \rho_a u_*^2$ , with  $\rho_a$  the density of the atmosphere at the surface and  $u_*$  the friction velocity (see Kok et al., 2012). Saltation, and hence erosion, is initiated when the wind stress is above a critical value. The saltation flux,  $Q$ , scales as  $Q \propto \tau_{\text{ex}} V$ , where  $\tau_{\text{ex}} = \tau_* - \tau_{*\text{it}}$  is the ‘excess’ stress,  $\tau_{*\text{it}}$  is the impact threshold stress – the minimum value required to sustain saltation – and  $V$  is the mean horizontal particle speed (see Kok et al. (2012) and Sullivan and Kok (2017) for more details). If  $V$  is assumed to increase linearly with  $u_*$  then  $Q \propto u_* \tau_{\text{ex}}$ , while if  $V$  is constant with  $u_*$  then  $Q \propto \tau_{\text{ex}}$ . Previous work has assumed a linear increase of  $V$  with  $u_*$  (e.g. White, 1979; Armstrong and Leovy, 2005; Almeida et al., 2008; Wang and Zheng, 2015), while recent work suggests the relation  $Q \propto \tau_{\text{ex}}$  should be used (Sullivan and Kok, 2017).

The timing of mound erosion (relative to atmospheric loss) is currently not well understood (Bennett and Bell, 2016), and nor is the climate at the time erosion might have occurred, as this can vary with orbital changes and atmospheric loss (e.g. Kite et al., 2014; Soto et al., 2015; Wordsworth, 2016; Ramirez, 2017). Partly for these reasons, and partly because it allows us to compare our model results to reality, all simulations presented here have surface pressures similar to those of present day Mars ( $\sim 6$  hPa). In general, the surface stresses predicted by our simulations are not large enough to initiate saltation, which is a situation that occurs in many other models (see Sullivan and Kok, 2017). As such, we do not use an explicit erosion relation, and simply compare the magnitudes of the surface wind stress across the craters and mounds, relating regions of higher stress with increased potential erosion.

### 3 Results

It is not possible to simulate the entire mound formation process with a mesoscale model, but such a model can be used to take ‘snapshots’ in time, to see how the circulation patterns would potentially erode the sediment within the crater. Initially we look at the circulation in axisymmetric craters with diameters of 40, 80 and 160 km. This spans most of the range of mound-hosting craters cataloged by Bennett and Bell (2016), with only the smallest craters missing. The craters are surrounded by flat topography, with the results azimuthally-averaged from radial slices taken every  $3^\circ$  (as in Tyler and Barnes, 2015). Later we also look at craters covered with thick sedimentary layers, and idealized craters embedded within realistic topography. In these cases the results are not azimuthally-averaged, as the topography is not axisymmetric.

### 3.1 Erosion in craters filled with sedimentary deposits

We begin by looking at mound formation in craters containing horizontally-level sedimentary deposits. For diameters of 40, 80 and 160 km, we assume sediment-free (basement) depths of 2.4, 3.5 and 5 km, corresponding to data for pristine Mars craters (Tornabene et al., 2018). For each diameter, we model craters with floors that are (i) level with the surrounding flat plains, so only the crater rim protrudes, and (ii) 1.75 km below the surrounding plains. For the 80 and 160 km diameter craters we also consider crater floors 3.5 km below the surrounding plains. These simulations represent different levels of sedimentary infill. We do not consider the possibility of a central peak (produced during crater formation) protruding from the sediment-filled craters. Instead we assume that if present, a central peak is below the sediment, either due to an initial small size, or through degradation (e.g. Robbins and Hynek, 2012; Tornabene et al., 2014).

Figure 4 shows results from the 160 km diameter simulations at (a–c) 14:00 and (d–f) 19:00 local time, as this is when the upslope winds and downslope winds (respectively) are typically at their strongest in these simulations (see Movie S1 in the supporting information for full diurnal results). Results from the smaller-diameter craters are similar, and are thus not shown. The shading shows the magnitude of the wind multiplied by the sign of the radial wind, i.e.  $u = (u_r/|u_r|)\sqrt{u_r^2 + u_v^2}$ , with  $u_r$  and  $u_v$  the radial and vertical components of the wind ( $u_r$  is typically an order of magnitude greater than  $u_v$ ).

For a given crater diameter, as the depth of the crater increases, the strength of the wind on the crater rim increases. This is caused by the larger temperature and hence pressure differences across the crater, as noted by Tyler and Barnes (2015). Figure 5 shows the surface wind stress for these three craters, as a function of time of day and distance from the crater center. As can be seen in Figure 5a, away from the non-erodible crater rim the largest values of surface wind stress occur on the crater floor in the evening (18:00–22:00), and are associated with air moving down the walls of the crater rim and towards the center, as seen in Figure 4d. The ‘lumpy’ appearance of the surface wind stress from 18:00–22:00 is a result of the discrete model output every 20 Mars minutes. For a crater filled with sediment with only the rim protruding as in Figure 5a, it is likely that passing synoptic weather systems and localized strong gusts would lead to more erosion than the nighttime downslope flow. This would likely increase the depth of the crater at all locations, though vortical flows may preferentially erode more sediment near the crater walls (Day et al., 2016; Anderson and Day, 2017).

In the case of a crater 1.75 km deep (Figures 4b,e and 5b), it is clear that on the erodible crater floor there are two daily periods of increased surface wind stress. There is again the 18:00–22:00 period associated with downslope winds which would likely erode all locations equally, but there is also now a period centered around 13:00, which is associated with upslope

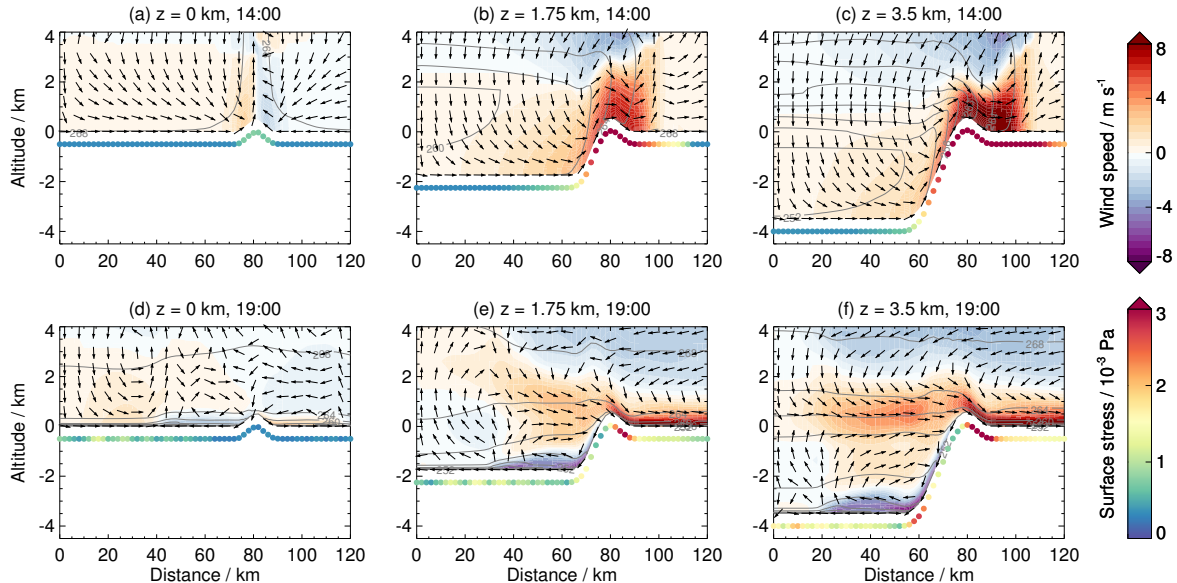


Figure 4: Azimuthally-averaged wind speed (shaded), wind direction (arrows) and potential temperature (contours) for three 160 km diameter craters with floors at different depths,  $z$ , below the surrounding plains (labeled above each plot). Plots show values at 14:00 (a–c) and 19:00 (d–f) local time, with colored circles showing the maximum daytime (08:00–17:00) and nighttime (17:00–08:00) surface wind stress values in the top and bottom rows respectively. Potential temperature is contoured at 2 K intervals in (a–c) and 4 K intervals in (d–f).

winds and has stress values increasing towards the crater wall. It should be noted that the stress values here result from grid box-average winds, which do not explicitly take gustiness into account. In general there is increased gustiness during the daytime (e.g. Fenton and Michaels, 2010), so peak surface wind stresses are likely to be higher than represented in the model. Even without taking this into account, erosion associated with a stress distribution like that in Figure 5b would result in more sediment being removed towards the base of the crater wall, with erosion decreasing with distance towards the center, forming a mound (assuming detachment-limited sediment transport). Erosion from traveling synoptic systems would likely be less important than for the filled case in Figure 5a, as craters get isolated from the surrounding environment as they get deeper (e.g. Rafkin et al., 2016).

At an even greater depth of 3.5 km (Figures 4c,f and 5c), the surface wind stress associated with the nighttime downslope wind has increased, mainly because of stronger winds (as can be seen in Figure 4f), but also due to the increasing atmospheric density in a deeper crater. However, now the stress during the daytime at the base of the crater wall is lower, and so the tendency to form a mound is reduced. Additional simulations at different depths were performed in order to understand this behavior, with the results shown in Figure 6. The surface wind stresses on the crater floor near the crater wall initially increase as the crater depth increases, up to  $\sim 2$  km, and then start to decrease again. This maximum is a result



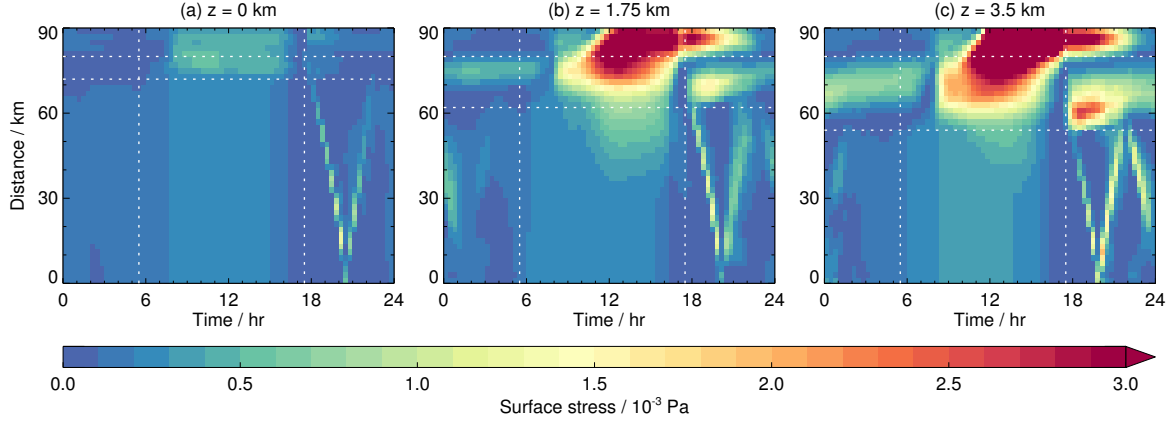


Figure 5: Surface wind stress, as a function of time of day (Mars hours) and distance from the crater center, for the three craters shown in Figure 4. Horizontal dotted lines mark the top and bottom of the crater wall, while vertical dotted lines show the sunrise and sunset times.

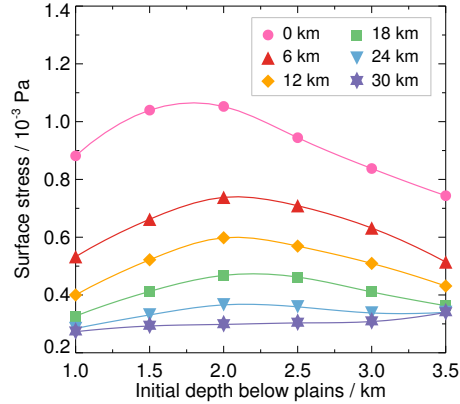


Figure 6: Variation of maximum daytime surface wind stress on the crater floor, as a function of distance from the crater wall (colored lines, ranging from 0–24 km). Values are shown for six 160 km diameter craters of different depths (1–3.5 km below the surrounding plains).

of two competing factors. Firstly, as the crater depth increases, the daytime air over the crater at the same level as the surrounding plains gets cooler, as can be seen by the potential temperature contours in Figure 4a–c. This results in a larger pressure difference, creating a stronger surge of air out of the crater at the rim (see Tyler and Barnes, 2015). The wind speed increases from the crater center to the rim, so initially as the depth increases the wind speeds and hence stress values on the crater floor increase. However, for crater walls of the same angle ( $10^\circ$  in these simulations), as the crater gets deeper the base of the wall moves closer to the crater center (see Figure 5), into a region of slower winds. These two competing factors result in the behavior seen in Figure 6, where a crater depth of  $\sim 2$  km is the most favorable for erosion by slope winds near the crater walls.

Similar behavior is seen in the simulations with diameters of 40 km and 80 km. Thus, it

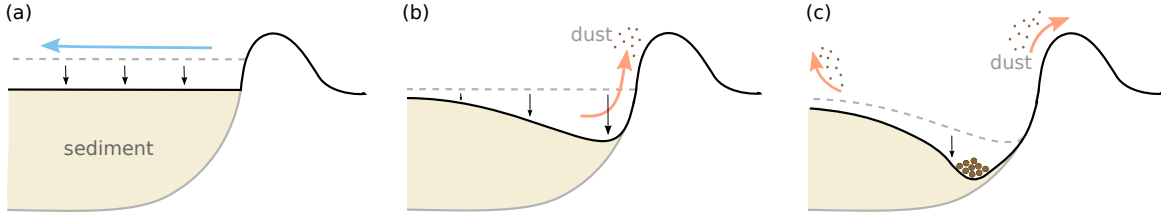


Figure 7: Cartoon showing the proposed evolution of a sediment filled crater, from initial level infill to mound formation. Red and blue arrows show the directions of the strongest daytime and nighttime winds respectively. Black arrows show how sediment erodes.

seems plausible that a mound can begin to form by slope wind erosion if a sediment-filled crater has a depth shallower than a certain value ( $\sim 2$  km in these idealized simulations). If a process results in the depth of the sediment-filled crater being much larger this value, then the reduced stress near the crater wall may result in either much slower mound formation, or possibly no mound formation at all if the threshold for sand transport is high. However, it may be possible for saltation to be initiated and maintained at lower wind speeds than the fluid threshold (Kok, 2010; Sullivan and Kok, 2017).

Figure 7 shows a cartoon of our proposed method of mound formation in craters with initial flat infill. Erosion from nighttime downslope winds, as well as daytime wind gusts and dust devils which are not modeled, initially results in a gradual deepening of the crater (Figure 7a). As the crater gets deeper it gets more isolated from the surrounding environment and the upslope and downslope flows on the crater wall increase in strength, preferentially eroding sediment close to the crater wall (Figure 7b). Small dust particles can remain suspended in the air, and can be transported away from the crater. However, larger abrading clasts may accumulate at the low points on the crater floor (Figure 7c). This may increase the erosion in these areas, such as in the case of potholing in rivers on Earth (e.g. Pelletier et al., 2015), leading to a positive feedback. Alternatively, a coarse-grained lag deposit can armor underlying softer rocks. Accumulations of larger particles in crater moats are observed, e.g. the Bagnold Dune Field in Gale crater (Hobbs et al., 2010; Charles et al., 2017).

### 3.2 Mound evolution

The results of the previous section suggest that mounds can form from craters with initial flat sedimentary infill. Thus, we next look at different mound profiles to see how they might evolve through wind erosion. Mound heights at a distance  $r$  from the crater center are given by  $h_{\text{mound}}(r) = h_{\text{max}} \cos(\pi r / 2r_{\text{max}})$ , where  $h_{\text{max}}$  is the maximum height of the mound, and  $r_{\text{max}}$  is the maximum radius of the mound (which is  $\leq$  the crater floor radius). This profile provides a good match to the average slope of Mt. Sharp.

### 3.2.1 Mounds in craters 1.75 km deep

We begin by considering two different mound shapes in craters of 40, 80 and 160 km diameter, and 1.75 km depth. The first mound profile begins at the base of the crater wall, and extends to 90% of the crater depth. A mound of this type might emerge if the surface wind stress and hence erosion were maximum at the base of the crater wall and decreased towards the crater center, as suggested by Figure 5b. As the mounds are the same height but the crater diameters differ, the sides of the mound get steeper as the diameter gets smaller. The circulation patterns at 14:00, and the peak daytime stresses for these mound shapes, are shown in Figure 8a–c (see Movie S2 in the supporting information for full diurnal results). As the crater diameter increases, the strength of the flow over the crater rim increases slightly, because of the larger temperature and hence pressure difference between the air over the crater and over the plains. Conversely, the upslope flow over the mound decreases in strength. This is because fractionally more air is lost from the smaller crater over the rim, resulting in increased downwelling, increased adiabatic warming of air in the crater, and stronger flow up the mound (see Tyler and Barnes, 2015). Due to the stronger winds blowing up the mound, the peak daytime surface wind stresses on the mound increase as crater diameter decreases. The peak stress values occur roughly 2/3 of the way up the mound in all cases. At the tops of the mounds, the peak stresses in the 40 and 80 km craters are larger than in the moat (Figure 8a,b), while in the 160 km crater the peak stress at the top of the mound is lower than in the moat.

Looking next at the circulation at 19:00, and the peak nighttime surface wind stresses (Figure 9a–c; see also Movie S2) it can be seen that while the downslope flows on the crater walls are similar, the strength of the flow on the mound increases as the crater diameter increases. This is because the smaller crater cools more quickly, so by 19:00 the potential temperature contours are aligned horizontally, while in the larger craters the potential temperature contours are still terrain-following. This larger horizontal potential temperature gradient sustains the downslope flow for longer, resulting in larger surface wind stresses, with the peak value in the largest crater occurring about 2/3 of the way down the slope (Figure 9c). In the smallest crater, the stresses are again larger towards the top of the mound compared to the moat (Figure 9a). Daytime and nighttime stress distributions such as these suggest that, if all other factors were held equal, the mounds in the 40 and 80 km craters would likely erode more at their tops than at their bases, eventually becoming more squat, while the mound in the 160 km crater would erode more at the sides and base than at the top, becoming steeper-sided. This may be one of the reasons why larger diameter craters have a greater frequency of mounds surrounded by moats (see Figure 3).

Figure 10 shows how mound heights in craters identified by Bennett and Bell (2016) compare to their host craters. Heights for each crater were determined by taking radial slices through MOLA 128 ppd data every  $0.5^\circ$ , and then calculating the maximum crater depth, the maxi-

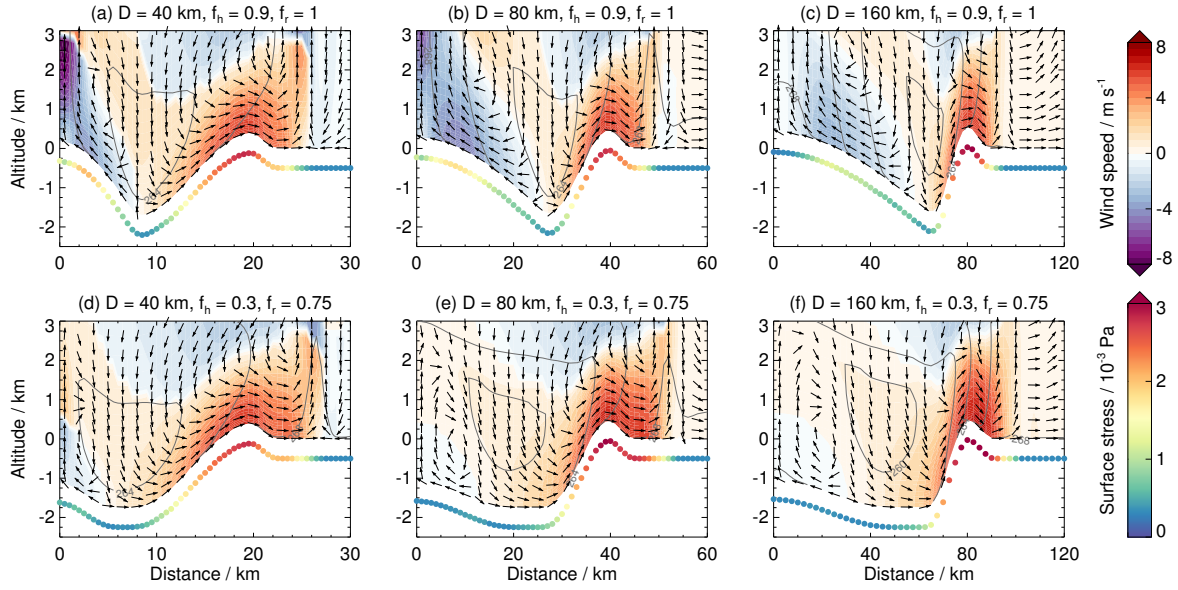


Figure 8: Azimuthally-averaged wind speed (shaded), wind direction (arrows) and potential temperature (contours) at 14:00 local time for craters with diameters of 40, 80 and 160 km, and with mounds of different fractional heights,  $f_h$ , and radii,  $f_r$ , (labeled above each plot, as fractions of the crater depth and crater floor radius). Colored circles show the maximum daytime (08:00–17:00) surface wind stress values. Potential temperature is contoured at 2 K intervals.

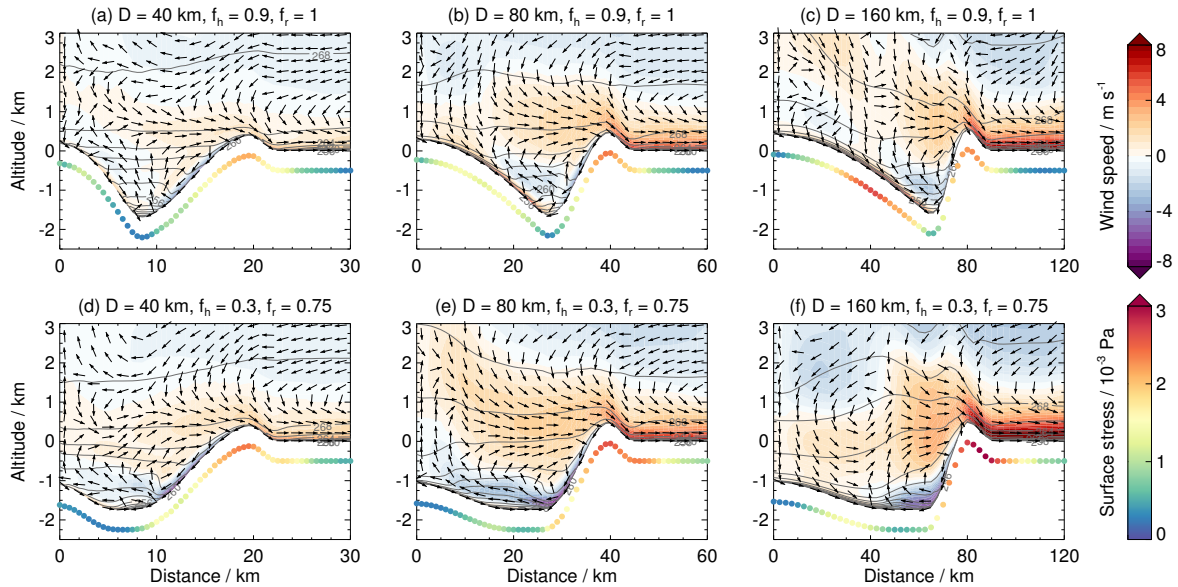


Figure 9: As Figure 8, but for 19:00 local time, with the colored circles showing the maximum nighttime (17:00–08:00) surface wind stress values.

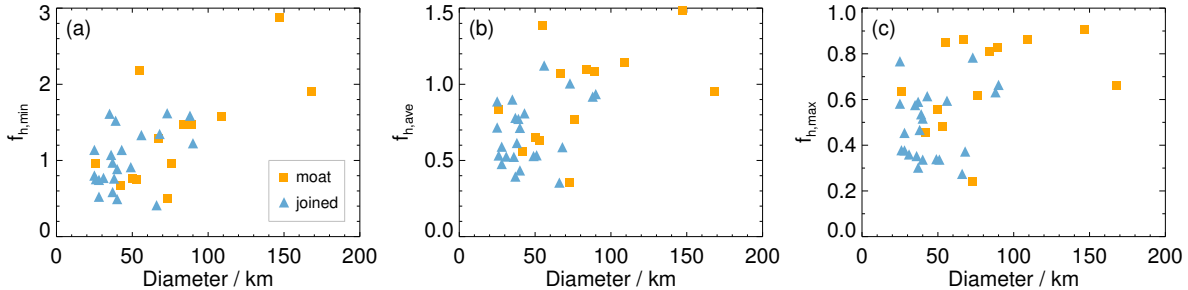


Figure 10: Mound heights expressed as a fraction of the distance between the crater floor and (a) the minimum, (b) the average, and (c) the maximum rim height. Data are for mound-hosting craters listed by Bennett and Bell (2016), with the mound and rim heights determined from MOLA 128 ppd data (errors are smaller than the symbol sizes).

imum mound height (ignoring central uplift peaks from crater formation), and the minimum, maximum and average rim heights. It can be seen that there is a tendency for smaller craters to have proportionally smaller mounds, suggesting more erosion of the mound tops. Indeed, from  $10^5$  Monte Carlo bootstrap trials fitting a linear trend line to Figure 10c, in only 36 cases did a negative slope result. This behavior is in agreement with the stress distributions, which show mounds in smaller craters experience greater surface wind stresses towards the tops of the mounds than do larger craters.

We now consider a much smaller mound that extends to 75% of the radius of the crater floor, and 30% of the crater depth. This morphology may be the result of erosion over a long time scale in a crater initially filled with sediment, or early erosion in a crater only filled with a small layer of sediment. During the daytime (Figure 8d–f; see also Movie S2) the upslope winds along the crater walls and out over the rim are slightly stronger than for the case with the larger mound (Figure 8a–c). This is because a smaller mound results in a greater volume of air within the crater, and a greater average distance between the crater floor/mound (which heats up rapidly during the day) and the air that is level with the surrounding plains. As such, the air is cooler by  $\sim 2\text{--}3\text{ K}$ , and hence there is a larger pressure difference driving the outward surge of air away from the crater.

As the smaller mounds sit lower in the crater, they are affected more by the downwelling and associated adiabatic warming discussed earlier, and hence near-surface temperatures are warmer than for the larger mounds. At the tops of the mounds, the temperatures are  $\sim 5\text{ K}$  warmer in the 40 km diameter crater, and  $\sim 2\text{ K}$  warmer in the 80 and 160 km diameter craters. However, the stronger downwelling and denser atmosphere results in weaker upslope winds on the mound flanks, and so surface wind stresses are lower ( $\sim 20\text{--}50\%$  of the values on the larger mounds). For the 40 km diameter crater the stress is still larger near the top of the mound than at the base, while in the 80 and 160 km diameter craters the stress values are similar along the mounds.

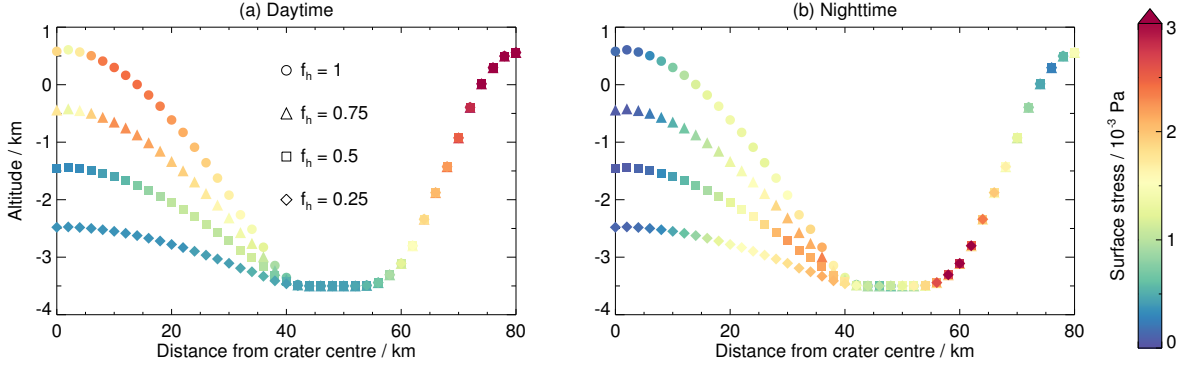


Figure 11: Maximum daytime and nighttime surface wind stress (colors) from simulations of craters 160 km in diameter and 3.5 km deep. The symbol locations show the mound profiles, where  $f_h$  denotes the fractional height of the mound in relation to the crater depth (the fractional radius is 0.7 in all cases).

By 19:00 (Figure 9d–f; see also Movie S2), near-surface temperatures over the mounds have cooled by around 10 K, and downslope winds are at their strongest. Surface wind stresses on the mound in the smallest crater show little variation, with a slight increase towards the top of the mound. In the 80 and 160 km diameter craters, the greater potential temperature difference near the mound flanks means downslope winds can exist for longer (as discussed earlier), resulting in stress values that increase towards the mound base. (The surface wind stresses are again  $\sim 20\text{--}50\%$  of the values on the larger mounds.) These results suggest that as the mounds become more eroded and exist deeper within the craters, the weaker near-surface circulation produces less erosion. This may explain why intra-crater mounds persist today, rather than wind erosion removing them completely.

### 3.2.2 Mounds in craters 3.5 km deep

We now briefly look at mounds in craters where the moat is 3.5 km below the surrounding plains, focusing on craters with diameters of 160 km. We consider mounds with radii extending to 70% of the crater floor radius, and heights ranging from 25% to 100% of the crater depth. The maximum daytime and nighttime surface wind stresses are shown in Figure 11. The circulation patterns are not shown, but follow the behavior seen in Figures 8c,f and 9c,f.

At the crater rim the temperature fields are nearly identical in the different simulations, and thus the daytime surges of air away from the craters are similar. Near-surface daytime temperatures increase as the mound height decreases (through adiabatic warming associated with downwelling) with temperatures over the shortest mound ( $f_h = 0.25$ ) being  $\sim 5$  K warmer than over the tallest mound ( $f_h = 1$ ). As for the 1.75 km deep craters, the upslope winds decrease in strength as the mounds become shorter, due to the combination of increased air

density and downwelling. As such, the surface wind stresses also decrease (Figure 11a). In the 160 km diameter, 1.75 km deep crater, the stress at the top of the mound was the lowest of any point within the crater (see Figure 8c). This is not true for the tallest two mounds in the 3.5 km deep case, where stronger winds at the mound tops produce stresses larger than in the moat.

At nighttime, the acceleration of the downslope winds causes the surface wind stress to increase towards the base of the mounds (Figure 11b). For the mounds with  $f_h = 0.25$  and  $f_h = 0.5$ , the nighttime stress values at the mound base are the largest of any time of day. Such mounds may be expected to erode more on the flanks and become steeper-sided. For the mound with  $f_h = 1$ , the maximum daytime stress from upslope winds is larger than the maximum nighttime value. Thus, this mound may be expected to erode more at the top, becoming more squat. If this were to occur, it may eventually reach a height where the stress was larger towards the base of the mound, and it would then erode more horizontally. (For the mound with  $f_h = 0.75$ , the maximum daytime and nighttime stress values are about equal.)

### 3.3 Erosion in craters covered with sedimentary deposits

So far we have considered erosion in axisymmetric craters filled with sediment and surrounded by flat topography. However, it has been suggested that some intra-crater mounds are the result of the erosion of large sedimentary deposits that existed on top of craters, particularly for mounds in the Arabia Terra region (Ferguson and Christensen, 2008; Bennett and Bell, 2016). We have therefore performed simulations of 40, 80 and 160 km diameter craters with a 1 km thick sedimentary layer partially covering the craters to different extents (to represent the gradual erosion and retreat of the layer over time). Figure 12 shows slices through the 160 km diameter craters to highlight the morphologies, and Figure 13 shows results for the same craters. In these simulations the sedimentary layer slopes in the east-west direction, with no variation in the north-south direction. The gradient is 0.06 (slope angle  $\sim 3.4^\circ$ ), which was chosen to be similar to the gradients of the sloping mounds seen in Figure 2a,b. Three nested grids are used, with an inner grid spacing of 5 km.

When the sedimentary layer covers almost the whole crater, leaving only the rim exposed, the meridional wind has little effect on the circulation, and it is the zonal wind blowing up and down the face of the sedimentary layer that causes the surface wind stress distributions (Figure 13a–d). As such, the layer would be expected recede to the east uniformly over time. We assume that as the layer recedes the sediment within the crater will also be eroded, deepening the crater. As such, we next model a crater where the sedimentary layer covers 3/4 of the crater diameter, and the crater depth has increased (Figure 13e–h). In this case, the daytime flow up the face of the layer is still generally uniform across the crater, but there is increased surface wind stress on top of the layer near the crater rim due to the zonal wind

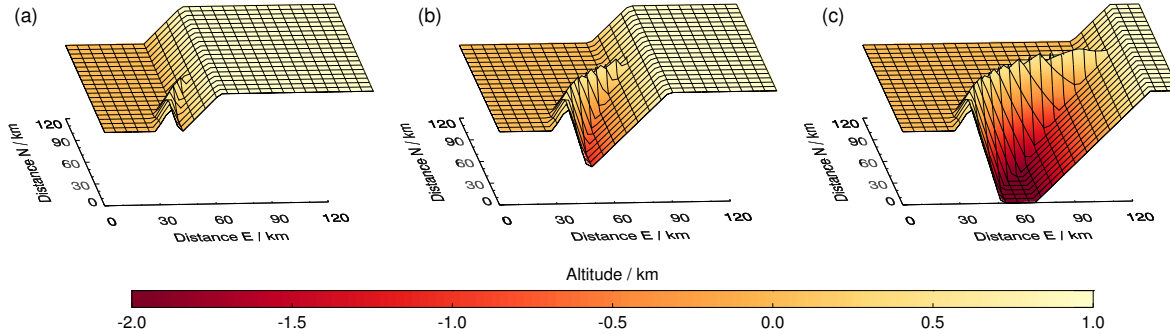


Figure 12: Morphologies of three 160 km diameter craters covered to different extents by a 1 km deep sedimentary layer. This represents the retreat of the layer over time from west to east. (Time evolution between the three morphologies is not considered.)

being funneled by the topography. During the evening and night, the downslope flow along the crater walls and sedimentary layer results in increased surface wind stresses towards the crater walls (Figure 13h). Similar behavior is seen for the case where the sedimentary layer covers half the crater (Figure 13i–l), with the deeper crater allowing for stronger downslope winds and increased stresses towards the crater walls (Figure 13l).

The surface wind stress patterns in these simulations suggest that as a sedimentary layer recedes across a crater, it will erode more at the edges of the crater, resulting in a crescent-shaped moat. The behavior shown for these 160 km diameter craters also occurs for 80 km diameter craters, but in the 40 km diameter simulations the behavior suggests just a linear retreat of the sedimentary layer, with no clear signal for the formation of a crescent-shaped moat. Wind tunnel experiments by Day et al. (2016) showed that a crescent-shaped moat can form if there is a uni-directional wind blowing across a crater. However, their experiments used 30 cm and 60 cm diameter crater models, and so the mound at all times is impacted by the prevailing wind. In large diameter craters, the mound could be many tens of kilometers away from the crater rim, lessening the impact of the large-scale wind blowing across the crater. However, large eddy simulations suggest that vortical flows can also result in crescent-shaped moats (Day et al., 2016; Anderson and Day, 2017). Thus, in smaller craters (< 40 km diameter) vortical flows can explain crescent-shaped moats, while in larger craters both vortical flows or the erosion of a covering sedimentary layer by slope winds are possible mechanisms.

### 3.4 Erosion in a realistic atmosphere

The simulations performed so far lack the Coriolis force, thermal tides, initial large-scale winds, and realistic topography. This was in order to isolate the topography-windfield coupling. To compare these idealized simulations with reality, we performed additional ‘realistic’



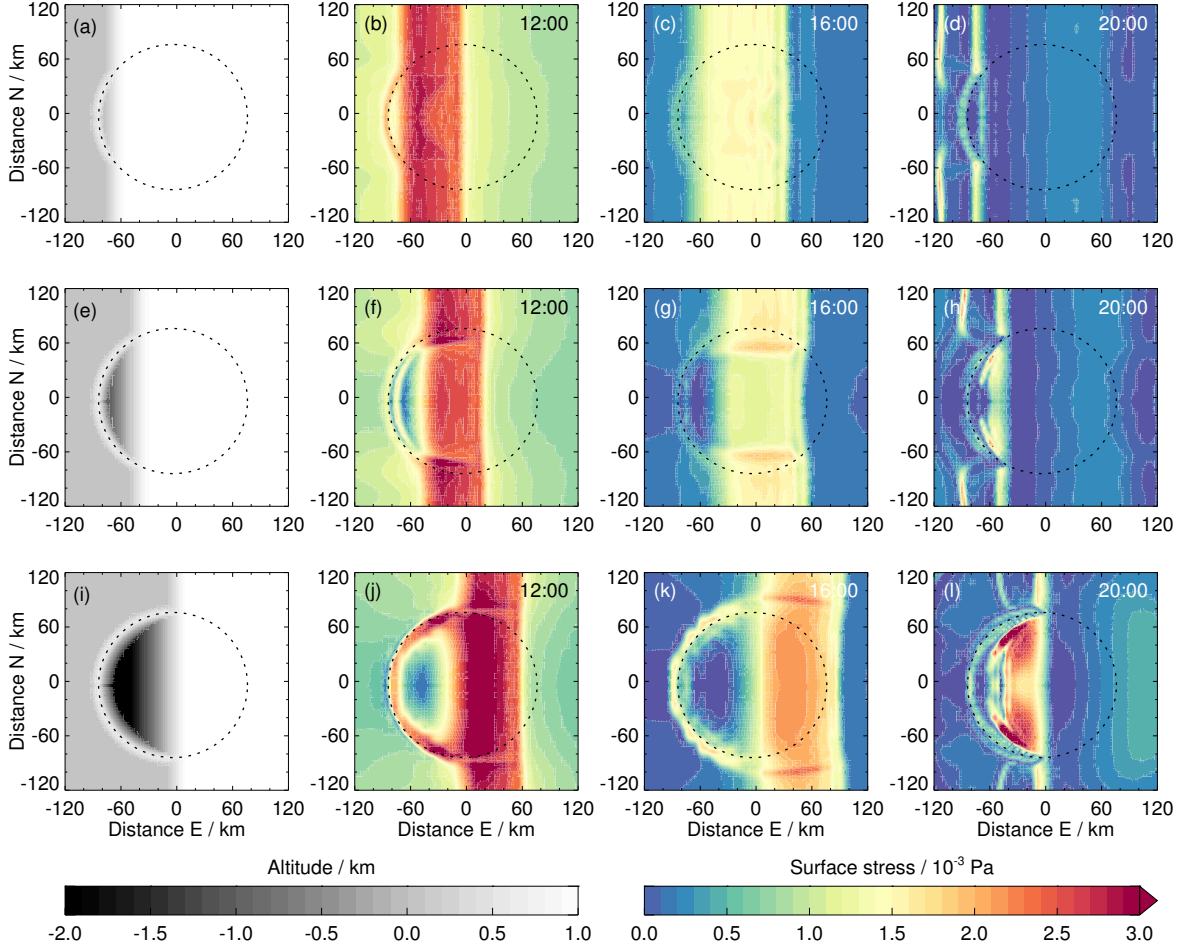


Figure 13: Topography (left column) and surface wind stress values at three different times (remaining columns) for three 160 km diameter craters covered to different extents by a 1 km thick sedimentary layer (each row shows a different crater morphology). The dotted line shows the location of the crater rim, and the local times are labeled on each panel.

simulations using GCM boundary conditions (see section 2 for a description of the method). An idealized axisymmetric crater (160 km in diameter and 3.5 km deep, with a mound covering 70% of the crater floor radius and the full depth of the crater) was placed at  $0^\circ\text{N}$ ,  $0^\circ\text{E}$  (see Figure 14). This is close to the region in Arabia Terra where mound-hosting craters are common (Lewis and Aharonson, 2014; Bennett and Bell, 2016; Tanaka, 2000; Hynek and Di Achille, 2017). Simulations were performed at four different times of year ( $L_S = 45^\circ$ ,  $135^\circ$ ,  $225^\circ$  and  $315^\circ$ ). Results are similar in all periods, and the results from  $L_S = 315^\circ$  are shown in Figure 15. (See Movies S3-S4 in the supporting information for full diurnal results at each  $L_S$ ).

It is evident that the behavior is similar to the idealized cases, with downslope winds at night and strong upslope winds during the afternoon which increase in strength as they travel up

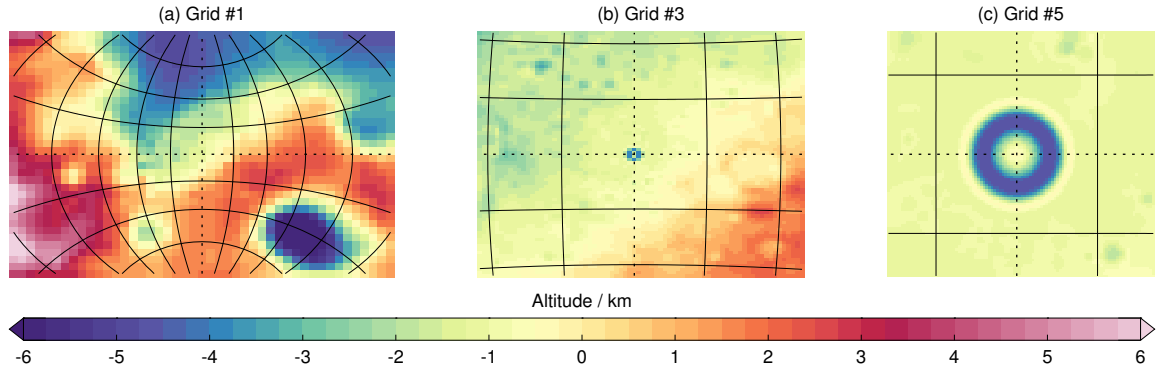


Figure 14: Topography on grids 1, 3 and 5 of the ‘realistic’ simulations (resolution 324, 36 and 4 km respectively). Black contours show the latitude and longitude in intervals of  $10^\circ$ ,  $5^\circ$  and  $2^\circ$  respectively. Dotted lines show  $0^\circ\text{N}$ ,  $0^\circ\text{E}$ .

the crater walls and mound flanks. The main difference is that the external wind field, which is strongest in the morning and afternoon, blowing from east to west (Figure 15b,c), causes the stress field to be non-axisymmetric. The effect of this wind field is to increase the surface wind stress on the western crater wall and the leeward slope of the mound. Figure 16 shows the circulation in a longitude-altitude plane taken across the center of the crater, with the times corresponding to those of Figure 15.

At 06:00 the downslope wind is strongest on the eastern crater wall, as the slope is oriented in the same direction as the prevailing wind. By 09:00 the upslope flow over the mound flanks has developed, and is stronger than the flow on the crater walls. By 12:00 the upslope flows are fully developed. At the top of the mound there is convergence of the upslope flow, and the air is transported upwards away from the crater (Figure 16c), resulting in lower surface wind stresses at the top of the mound (Figure 15c). At this time the upslope flow is strongest on the leeward slope of the mound. This is because the windward slope is affected by the prevailing wind, which, by the time it arrives at the mound, is traveling westward and downward. The subsiding component results in adiabatic warming, and thus the temperature contrast between the mound flank and the surrounding air is reduced (compare the potential temperature contours on either side of the mound in Figure 16c), limiting the strength of the upslope flow on the mound. The leeward slope is shielded from the prevailing easterly wind, and so the air temperatures are cooler, there is a larger temperature contrast between the mound flank and the surrounding air, and the upslope flow (and hence surface wind stress) can become stronger.

By contrast, Day et al. (2016) found that the mound in their wind tunnel experiments was preferentially eroded on the windward flank. However, as noted earlier, the size of their model crater means the mound is more likely to feel the direct effects of the wind, and be eroded. Additionally, such small models cannot take into account the changes in temperature

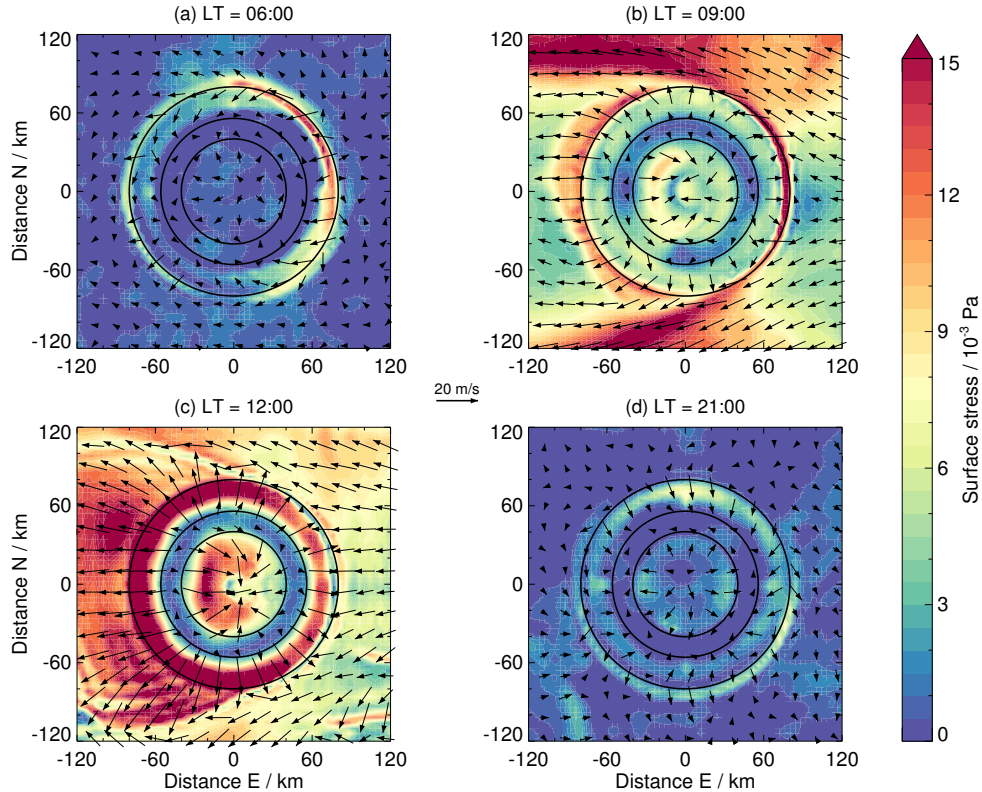


Figure 15: Surface wind stress (shading) at four different local times from a simulation of a 160 km diameter and 3.5 km deep axisymmetric crater at  $L_S = 315^\circ$ . Arrows show the wind speed and direction, while the three black circles denote the locations of the crater rim and the bases of the crater and mound walls.

experienced within real craters. Again, the mechanism inferred by Day et al. (2016) may occur in smaller diameter craters, while mounds in larger diameter craters may experience different erosional patterns. An example of such a case is Gale crater, where Mt. Sharp is offset in the opposite direction to the prevailing wind direction (Bennett and Bell, 2016), which is the behavior suggested by the erosion patterns in our simulations. Indeed, if erosion follows the surface wind stress field shown in Figure 15c, then our work suggests an explanation for the ‘bat-wing’ shape of Mt. Sharp.

## 4 Discussion

Our results show that winds on topographic slopes can potentially erode intra-crater sedimentary deposits to produce mounds. Mound evolution depends on the size of the host crater, with erosion in smaller craters resulting in mounds that are more squat, and erosion in larger craters resulting in steeper-sided mounds surrounded by moats. This behavior agrees with the mound morphologies in craters mapped by Bennett and Bell (2016). If craters are ini-

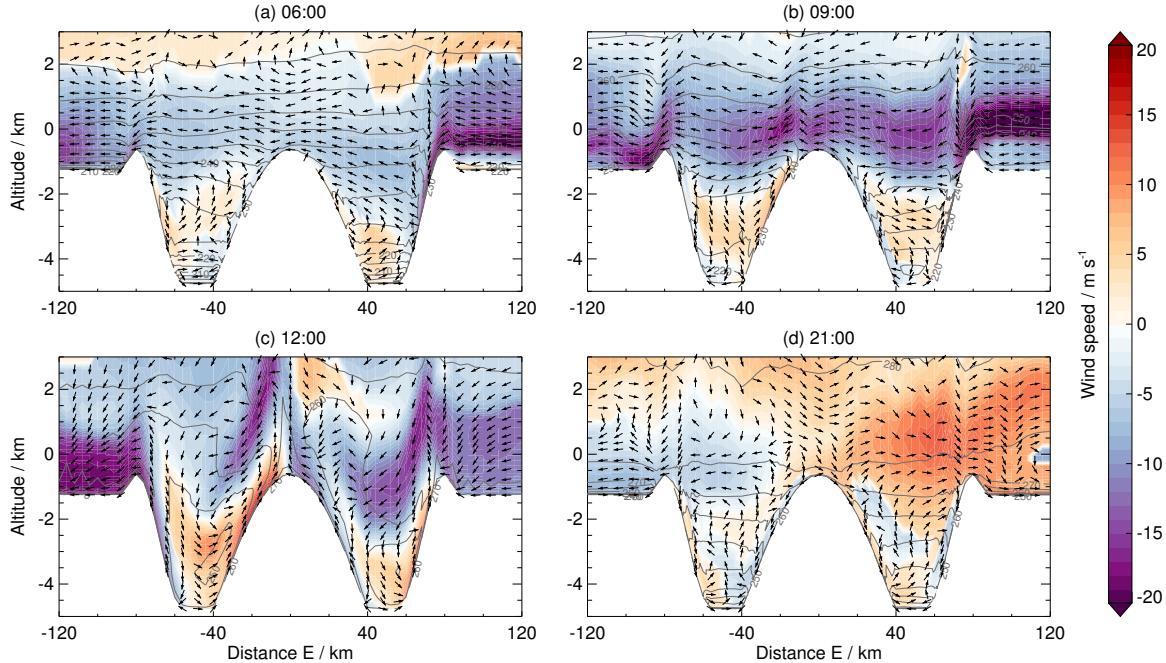


Figure 16: Wind speed (shaded), wind direction (arrows) and potential temperature (contours) at four different times from longitude-altitude slices through the center of the crater shown in Figure 15 in an east-west direction. Potential temperature is contoured at 5 K intervals.

tially covered in sedimentary layers, more complex erosion patterns emerge, and can result in crescent-shaped moats with mounds joined partly to the crater rim. Large-scale winds blowing over large mound-hosting craters can result in the mound eroding more on the leeward side, with the center of the mound appearing to ‘march upwind’ over time. This would result in a mound offset towards the direction of the prevailing wind, such as is observed for Mt. Sharp in Gale crater. Due to the strong day/night cycle of slope winds within canyons (e.g. Kite et al., 2016), the results presented here may also apply to the formation of mounds within canyon systems such as Valles Marineris.

Implicit in these results is that saltation-abrasion is the landscape-modifying mechanism. We do not consider other processes that may have operated in a warmer or wetter environment, as erosion by liquid water has not been globally significant since the Late Noachian/Early Hesperian (Golombek et al., 2006). We assume detachment-limited erosion, i.e. that the timescale for weathering the sediment is much longer than the timescale to transport sediment out of the crater, and thus we do not follow the motion of individual particles. We know that small dust particles can remain suspended in the atmosphere of Mars in the present day, so it is likely that over time attrition will result in sedimentary particles becoming smaller, at which point they can be transported away from the crater in the daytime upslope winds. Larger abrading clasts may remain in the crater moat, as is evidenced in the Bagnold Dune Field in Gale crater (Hobbs et al., 2010; Charles et al., 2017). Behavior such as this might

result in increased erosion of the moat, resulting in a positive feedback mechanism.

The simulations performed here are for atmospheric conditions relevant to present-day Mars, whereas much of the erosion of sedimentary mounds likely occurred billions of years ago (Thomson et al., 2011; Palucis et al., 2016; Kite and Mayer, 2017) when the atmosphere may have been much more dense (Jakosky et al., 2017). However, the main features noted here that are responsible for the erosion – the upslope and downslope winds – will still occur in a denser atmosphere. For example, slope winds are a common feature on Earth (e.g. Renfrew and Anderson, 2006; Whiteman et al., 2010; Haiden et al., 2011; Muñoz et al., 2013; Villagrasa et al., 2013; Lehner et al., 2016; Shapiro et al., 2016). Indeed, the diurnal variation of temperature profiles within Meteor Crater in Arizona (Whiteman et al., 2010) is similar to that in our simulations. However, in small craters like Meteor Crater, the strength of slope flows is limited due to the shallow depth, and so erosion is likely to be caused by smaller-scale features, such as those noted in large eddy simulations (Day et al., 2016; Anderson and Day, 2017). Thus, the main features and processes noted here are still likely to occur in a denser Martian atmosphere, though the strength of the winds, and hence the potential erosion rates, are likely to differ.

It should also be noted that there are features of the circulation not modeled here, and which may potentially affect erosion over long timescales. For example, dust devil tracks have been observed in many craters (Reiss et al., 2016), and dust devils have been detected in-situ by rovers in Gusev and Gale crater (e.g. Greeley et al., 2006, 2010; Moores et al., 2015; Kahanpää et al., 2016; Steakley and Murphy, 2016; Ordonez-Etxeberria et al., 2018). However, simulations of crater circulations have shown that the boundary layer is suppressed within craters (e.g. Tyler and Barnes, 2015; Rafkin et al., 2016), which should limit the formation of dust devils in deep craters (indeed, fewer were detected in Gale crater compared to the shallower Gusev crater). Thus, while convective vortices have the ability to remove dust from the surface (e.g. Balme and Greeley, 2006; Balme and Hagermann, 2006; Neakrase et al., 2016; Koester and Wurm, 2017), it is unlikely that dust devils contribute greatly to erosion rates within craters in the present-day. This may have been different in past climates, however (Newman et al., 2005; Haberle et al., 2006).

In the future, our ideas could be tested and refined by better constraints on erosion rates and patterns using crater counts (Kite and Mayer, 2017) and cosmogenic isotope exhumation-age dating (Farley et al., 2014).

## 5 Conclusions

While sedimentary mounds exist in craters of many different sizes, data (Bennett and Bell, 2016) suggest that there is a tendency for intra-crater mounds completely encircled by moats to

become more frequent as the crater diameter increases, hinting at a characteristic length scale (crater diameter) for encircling moats. We have performed mesoscale simulations considering craters 40, 80 and 160 km in diameter, with depths extending to 3.5 km, and a variety of mound and crater morphologies, to understand the formation of these sedimentary mounds.

1. Using a physically self-consistent numerical model, we find that mounds can form through wind erosion from craters surrounded by flat topography and filled with sediment. For a crater that is shallow, erosion will be fairly constant across the crater floor, resulting in an increase in the crater depth. As the depth increases to  $\sim 2$  km, slope winds become more important, and result in increased erosion near the crater walls, forming a mound. However, if the sediment-filled crater is much deeper than  $\sim 2$  km, the erosion near the crater walls reduces, and mound formation would either slow or stop completely.
2. Once a mound has formed, its evolution depends on the size of the host crater and its depth within the crater. For craters 40 and 80 km in diameter, the surface wind stress distributions in the simulations (used as a proxy for erosion) suggest that mounds would erode more at their tops than at their bases, eventually becoming flatter. Conversely, mounds in the 160 km crater would erode more at the sides and base than at the top, becoming thinner. This behavior is in agreement with observations: smaller craters tend to have proportionally shorter mounds. As mounds become more eroded and exist deeper in the crater, the weaker near-surface circulation reduces the surface wind stress, limiting the erosion. This may help to explain why mounds persist rather than being completely obliterated.
3. In the case of a large-scale sedimentary layer covering the craters (e.g. Ferguson and Christensen, 2008; Bennett and Bell, 2016) the surface wind stress patterns in the simulations suggest that as the sedimentary layer recedes across a crater, it will erode more towards the edges of the crater, which could explain the appearance of some of the mounds that are still joined to the crater wall.
4. When considering more realistic (GCM) meteorological boundary conditions, the main difference compared to the idealized simulations is the presence of a large-scale prevailing wind. The effect of this wind is to increase the surface wind stress values on the leeward side of the mound. The reason for this is that downwelling air on the windward side limits the strength of the daytime upslope flow. The leeward side experiences less downwelling air, and so the upslope wind can become stronger, increasing the surface wind stress and hence potential erosion. While most mounds are offset in the direction of the prevailing wind (Bennett and Bell, 2016), Mt. Sharp is offset in the opposite direction. The behavior in our simulations may offer an explanation for this offset, and for the ‘bat-wing’ shape of Mt. Sharp.

## Acknowledgments

We thank Mackenzie Day and an anonymous reviewer for their helpful comments which improved this paper. We thank Jasper Kok and Rob Sullivan for discussions of saltation on Mars, Daniel Tyler and Jeffrey Barnes for providing simulation results for benchmarking our model, Scot Rafkin for providing assistance with simulations, and the University of Chicago Research Computing Center. This work was funded in part by NASA grant NNX15AH998G. Model output is available to download from [https://psd-repo.uchicago.edu/kite-lab/mesoscale\\_crater\\_data](https://psd-repo.uchicago.edu/kite-lab/mesoscale_crater_data).

## References

- Almeida, M. P., Parteli, E. J. R., Andrade, J. S., Herrmann, H. J., 2008. Giant saltation on Mars. *Proc. Natl. Acad. Sci.* 105, 6222–6226.
- Anderson, R. B., Bell, III, J. F., 2010. Geologic mapping and characterization of Gale Crater and implications for its potential as a Mars Science Laboratory landing site. *Mars* 5, 76–128.
- Anderson, W., Day, M., 2017. Turbulent flow over craters on Mars: Vorticity dynamics reveal aeolian excavation mechanism. *Phys. Rev. E.* 96, 043110.
- Andrews-Hanna, J. C., Zuber, M. T., Arvidson, R. E., Wiseman, S. M., 2010. Early Mars hydrology: Meridiani playa deposits and the sedimentary record of Arabia Terra. *J. Geophys. Res. (Planets)* 115, E06002.
- Armstrong, J. C., Leovy, C. B., 2005. Long term wind erosion on Mars. *Icarus* 176, 57–74.
- Balme, M., Greeley, R., 2006. Dust devils on Earth and Mars. *Reviews of Geophysics* 44, RG3003.
- Balme, M., Hagermann, A., 2006. Particle lifting at the soil-air interface by atmospheric pressure excursions in dust devils. *Geophys. Res. Lett.* 33, L19S01.
- Bennett, K. A., Bell, J. F., 2016. A global survey of martian central mounds: Central mounds as remnants of previously more extensive large-scale sedimentary deposits. *Icarus* 264, 331–341.
- Bradley, B. A., Sakimoto, S. E. H., Frey, H., Zimbelman, J. R., 2002. Medusae Fossae Formation: New perspectives from Mars Global Surveyor. *J. Geophys. Res. (Planets)* 107, 2–1.
- Bridges, N. T., Ayoub, F., Avouac, J.-P., Leprince, S., Lucas, A., Mattson, S., 2012. Earth-like sand fluxes on Mars. *Nature* 485, 339–342.

- Bridges, N. T., Calef, F. J., Hallet, B., Herkenhoff, K. E., Lanza, N. L., Le Mouélic, S., Newman, C. E., Blaney, D. L., Pablo, M. A., Kocurek, G. A., Langevin, Y., Lewis, K. W., Mangold, N., Maurice, S., Meslin, P.-Y., Pinet, P., Renno, N. O., Rice, M. S., Richardson, M. E., Sautter, V., Sletten, R. S., Wiens, R. C., Yingst, R. A., 2014. The rock abrasion record at Gale Crater: Mars Science Laboratory results from Bradbury Landing to Rocknest. *J. Geophys. Res. (Planets)* 119, 1374–1389.
- Brothers, T. C., Holt, J. W., 2016. Three-dimensional structure and origin of a 1.8 km thick ice dome within Korolev Crater, Mars. *Geophys. Res. Lett.* 43, 1443–1449.
- Brothers, T. C., Holt, J. W., Spiga, A., 2013. Orbital radar, imagery, and atmospheric modeling reveal an aeolian origin for Abalos Mensa, Mars. *Geophys. Res. Lett.* 40, 1334–1339.
- Burbank, D. W., Anderson, R. S., 2011. *Tectonic Geomorphology*. John Wiley & Sons, Ltd.
- Chan, M. A., Netoff, D. I., 2017. A terrestrial weathering and wind abrasion analog for mound and moat morphology of Gale crater, Mars. *Geophys. Res. Lett.* 44, 4000–4007.
- Charles, H., Titus, T., Hayward, R., Edwards, C., Ahrens, C., 2017. Comparison of the mineral composition of the sediment found in two Mars dunefields: Ogygis Undae and Gale crater - three distinct endmembers identified. *Earth Planet. Sci. Lett.* 458, 152–160.
- Chipera, S. J., Vaniman, D. T., 2007. Experimental stability of magnesium sulfate hydrates that may be present on Mars. *Geochim. Cosmochim. Acta* 71, 241–250.
- Chojnacki, M., Burr, D. M., Moersch, J. E., Michaels, T. I., 2011. Orbital observations of contemporary dune activity in Endeavor crater, Meridiani Planum, Mars. *J. Geophys. Res. (Planets)* 116, E00F19.
- Conway, S. J., Hovius, N., Barnie, T., Besserer, J., Le Mouélic, S., Orosei, R., Read, N. A., 2012. Climate-driven deposition of water ice and the formation of mounds in craters in Mars' north polar region. *Icarus* 220, 174–193.
- Day, M., Anderson, W., Kocurek, G., Mohrig, D., 2016. Carving intracrater layered deposits with wind on Mars. *Geophys. Res. Lett.* 43, 2473–2479.
- Day, M., Kocurek, G. 2016. Observations of an aeolian landscape: From surface to orbit in Gale Crater. *Icarus* 280, 37–71.
- Farley, K. A., Malespin, C., Mahaffy, P., Grotzinger, J. P., Vasconcelos, P. M., Milliken, R. E., Malin, M., Edgett, K. S., Pavlov, A. A., Hurowitz, J. A., et al., 2014. In Situ Radiometric and Exposure Age Dating of the Martian Surface. *Science* 343, 1247166.
- Fenton, L. K., 2006. Dune migration and slip face advancement in the Rabe Crater dune field, Mars. *Geophys. Res. Lett.* 33, L20201.



- Fenton, L. K., Michaels, T. I., 2010. Characterizing the sensitivity of daytime turbulent activity on Mars with the MRAMS LES: Early results. *Mars* 5, 159–171.
- Ferguson, R. L., Christensen, P. R., 2008. Formation and erosion of layered materials: Geologic and dust cycle history of eastern Arabia Terra, Mars. *J. Geophys. Res. (Planets)* 113, E12001.
- Forget, F., Hourdin, F., Fournier, R., Hourdin, C., Talagrand, O., Collins, M., Lewis, S. R., Read, P. L., Huot, J.-P., 1999. Improved general circulation models of the Martian atmosphere from the surface to above 80 km. *J. Geophys. Res.* 104, 24155–24176.
- Golombek, M. P., Grant, J. A., Crumpler, L. S., Greeley, R., Arvidson, R. E., Bell, J. F., Weitz, C. M., Sullivan, R., Christensen, P. R., Soderblom, L. A., Squyres, S. W., 2006. Erosion rates at the Mars Exploration Rover landing sites and long-term climate change on Mars. *J. Geophys. Res. (Planets)* 111, E12S10.
- Golombek, M. P., Warner, N. H., Ganti, V., Lamb, M. P., Parker, T. J., Ferguson, R. L., Sullivan, R., 2014. Small crater modification on Meridiani Planum and implications for erosion rates and climate change on Mars. *J. Geophys. Res. (Planets)* 119, 2522–2547.
- Grant, J. A., Parker, T. J., Crumpler, L. S., Wilson, S. A., Golombek, M. P., Mittlefehldt, D. W., 2016. The degradational history of Endeavour crater, Mars. *Icarus* 280, 22–36.
- Greeley, R., Arvidson, R. E., Barlett, P. W., Blaney, D., Cabrol, N. A., Christensen, P. R., Ferguson, R. L., Golombek, M. P., Landis, G. A., Lemmon, M. T., McLennan, S. M., Maki, J. N., Michaels, T., Moersch, J. E., Neakrase, L. D. V., Rafkin, S. C. R., Richter, L., Squyres, S. W., de Souza, P. A., Sullivan, R. J., Thompson, S. D., Whelley, P. L., 2006. Gusev crater: Wind-related features and processes observed by the Mars Exploration Rover Spirit. *J. Geophys. Res. (Planets)* 111, E02S09.
- Greeley, R., Waller, D. A., Cabrol, N. A., Landis, G. A., Lemmon, M. T., Neakrase, L. D. V., Pendleton Hoffer, M., Thompson, S. D., Whelley, P. L., 2010. Gusev Crater, Mars: Observations of three dust devil seasons. *J. Geophys. Res. (Planets)* 115, E00F02.
- Grindrod, P. M., Warner, N. H., 2014. Erosion rate and previous extent of interior layered deposits on Mars revealed by obstructed landslides. *Geology* 42, 795–798.
- Haberle, R. M., Kahre, M. A., Murphy, J. R., Christensen, P. R., Greeley, R., 2006. Role of dust devils and orbital precession in closing the Martian dust cycle. *Geophys. Res. Lett.* 33, L19S04.
- Haiden, T., Whiteman, C. D., Hoch, S. W., Lehner, M., 2011. A Mass Flux Model of Nocturnal Cold-Air Intrusions into a Closed Basin. *J. Appl. Meteor. Climatol.* 50, 933–943.

- Hobbs, S. W., Paull, D. J., Bourke, M. C., 2010. Aeolian processes and dune morphology in Gale Crater. *Icarus* 210, 102–115.
- Holt, J. W., Fishbaugh, K. E., Byrne, S., Christian, S., Tanaka, K., Russell, P. S., Herkenhoff, K. E., Safaeinili, A., Putzig, N. E., Phillips, R. J., 2010. The construction of Chasma Boreale on Mars. *Nature* 465, 446–449.
- Hynek, B. M., Di Achille, G., 2017. Geologic map of Meridiani Planum, Mars (ver. 1.1, April 2017): U.S. Geological Survey Scientific Investigations Map 3356, pamphlet 9 p., scale 1:2,000,000.
- Hynek, B. M., Phillips, R. J., Arvidson, R. E., 2003. Explosive volcanism in the Tharsis region: Global evidence in the Martian geologic record. *J. Geophys. Res. (Planets)* 108, 15–1.
- Jakosky, B. M., Slipski, M., Benna, M., Mahaffy, P., Elrod, M., Yelle, R., Stone, S., Alsaeed, N., 2017. Mars' atmospheric history derived from upper-atmosphere measurements of  $^{38}\text{Ar}/^{36}\text{Ar}$ . *Science* 355, 1408–1410.
- Kahanpää, H., Newman, C., Moores, J., Zorzano, M.-P., Martín-Torres, J., Navarro, S., Lepinette, A., Cantor, B., Lemmon, M. T., Valentín-Serrano, P., Ullán, A., Schmidt, W., 2016. Convective vortices and dust devils at the MSL landing site: Annual variability. *J. Geophys. Res. (Planets)* 121, 1514–1549.
- Kite, E. S., Lewis, K. W., Lamb, M. P., Newman, C. E., Richardson, M. I., 2013. Growth and form of the mound in Gale Crater, Mars: Slope wind enhanced erosion and transport. *Geology* 41, 543–546.
- Kite, E. S., Mayer, D. P., 2017. Mars sedimentary rock erosion rates constrained using crater counts, with applications to organic-matter preservation and to the global dust cycle. *Icarus* 286, 212–222.
- Kite, E. S., Sneed, J., Mayer, D. P., Lewis, K. W., Michaels, T. I., Hore, A., Rafkin, S. C. R., 2016. Evolution of major sedimentary mounds on Mars: Buildup via anticompensational stacking modulated by climate change. *J. Geophys. Res. (Planets)* 121, 2282–2324.
- Kite, E. S., Williams, J.-P., Lucas, A., Aharonson, O., 2014. Low palaeopressure of the martian atmosphere estimated from the size distribution of ancient craters. *Nat. Geosci.* 7, 335–339.
- Koester, M., Wurm, G., 2017. Lifting particles in martian dust devils by pressure excursions. *Planet. Space Sci.* 145, 9–13.
- Kok, J. F., 2010. Difference in the Wind Speeds Required for Initiation versus Continuation of Sand Transport on Mars: Implications for Dunes and Dust Storms. *Phys. Rev. Lett.* 104 (7), 074502.

- Kok, J. F., Parteli, E. J. R., Michaels, T. I., Karam, D. B., 2012. The physics of wind-blown sand and dust. *Rep. Prog. Phys.* 75 (10), 106901.
- Lehner, M., Rotunno, R., Whiteman, C. D., 2016. Flow Regimes over a Basin Induced by Upstream Katabatic Flows - An Idealized Modeling Study. *J. Atmos. Sci.* 73, 3821–3842.
- Levy, J. S., Fassett, C. I., Head, J. W., 2016. Enhanced erosion rates on Mars during Amazonian glaciation. *Icarus* 264, 213–219.
- Lewis, K. W., Aharonson, O., 2014. Occurrence and origin of rhythmic sedimentary rocks on Mars. *J. Geophys. Res. (Planets)* 119, 1432–1457.
- Malin, M. C., Edgett, K. S., 2000. Sedimentary Rocks of Early Mars. *Science* 290, 1927–1937.
- Michaels, T. I., 2006. Numerical modeling of Mars dust devils: Albedo track generation. *Geophys. Res. Lett.* 33, L19S08.
- Michaels, T. I., Colaprete, A., Rafkin, S. C. R., 2006. Significant vertical water transport by mountain-induced circulations on Mars. *Geophys. Res. Lett.* 33, L16201.
- Michaels, T. I., Rafkin, S. C. R., 2008. Meteorological predictions for candidate 2007 Phoenix Mars Lander sites using the Mars Regional Atmospheric Modeling System (MRAMS). *J. Geophys. Res. (Planets)* 113, E00A07.
- Milliken, R. E., Grotzinger, J. P., Thomson, B. J., 2010. Paleoclimate of Mars as captured by the stratigraphic record in Gale Crater. *Geophys. Res. Lett.* 37, L04201.
- Moores, J. E., Lemmon, M. T., Kahanpää, H., Rafkin, S. C. R., Francis, R., Pla-Garcia, J., Bean, K., Haberle, R., Newman, C., Mischna, M., Vasavada, A. R., de la Torre Juárez, M., Rennó, N., Bell, J., Calef, F., Cantor, B., McConnochie, T. H., Harri, A.-M., Genzer, M., Wong, M. H., Smith, M. D., Martín-Torres, F. J., Zorzano, M.-P., Kempainen, O., McCullough, E., 2015. Observational evidence of a suppressed planetary boundary layer in northern Gale Crater, Mars as seen by the Navcam instrument onboard the Mars Science Laboratory rover. *Icarus* 249, 129–142.
- Muñoz, R. C., Falvey, M. J., Araya, M., Jacques-Coper, M., 2013. Strong Down-Valley Low-Level Jets over the Atacama Desert: Observational Characterization. *J. Appl. Meteor. Climatol.* 52, 2735–2752.
- Neakrase, L. D. V., Balme, M. R., Esposito, F., Kelling, T., Klose, M., Kok, J. F., Marticorena, B., Merrison, J., Patel, M., Wurm, G., 2016. Particle Lifting Processes in Dust Devils. *Solar Sys. Res.* 203, 347–376.
- Newman, C. E., Gómez-Elvira, J., Marin, M., Navarro, S., Torres, J., Richardson, M. I., Battalio, J. M., Guzewich, S. D., Sullivan, R., de la Torre, M., Vasavada, A. R., Bridges,

- N. T., 2017. Winds measured by the Rover Environmental Monitoring Station (REMS) during the Mars Science Laboratory (MSL) rover's Bagnold Dunes Campaign and comparison with numerical modeling using MarsWRF. *Icarus* 291, 203–231.
- Newman, C. E., Lewis, S. R., Read, P. L., 2005. The atmospheric circulation and dust activity in different orbital epochs on Mars. *Icarus* 174, 135–160.
- Ordóñez-Etxeberria, I., Hueso, R., Sánchez-Lavega, A., 2018. A systematic search of sudden pressure drops on Gale crater during two Martian years derived from MSL/REMS data. *Icarus* 299, 308–330.
- Palucis, M. C., Dietrich, W. E., Williams, R. M. E., Hayes, A. G., Parker, T., Sumner, D. Y., Mangold, N., Lewis, K., Newsom, H., 2016. Sequence and relative timing of large lakes in Gale crater (Mars) after the formation of Mount Sharp. *J. Geophys. Res. (Planets)* 121, 472–496.
- Pelletier, J. D., Sweeney, K. E., Roering, J. J., Finnegan, N. J., 2015. Controls on the geometry of potholes in bedrock channels. *Geophys. Res. Lett.* 42, 797–803.
- Pla-García, J., Rafkin, S. C. R., Kahre, M., Gómez-Elvira, J., Hamilton, V. E., Navarro, S., Torres, J., Marín, M., Vasavada, A. R., 2016. The meteorology of Gale crater as determined from rover environmental monitoring station observations and numerical modeling. Part I: Comparison of model simulations with observations. *Icarus* 280, 103–113.
- Putzig, N. E., Mellon, M. T., 2007. Apparent thermal inertia and the surface heterogeneity of Mars. *Icarus* 191, 68–94.
- Rafkin, S. C. R., 2009. A positive radiative-dynamic feedback mechanism for the maintenance and growth of Martian dust storms. *J. Geophys. Res. (Planets)*, E01009.
- Rafkin, S. C. R., Haberle, R. M., Michaels, T. I., 2001. The Mars Regional Atmospheric Modeling System: Model Description and Selected Simulations. *Icarus* 151, 228–256.
- Rafkin, S. C. R., Michaels, T. I., 2003. Meteorological predictions for 2003 Mars Exploration Rover high-priority landing sites. *J. Geophys. Res. (Planets)* 108, 8091.
- Rafkin, S. C. R., Pla-García, J., Kahre, M., Gómez-Elvira, J., Hamilton, V. E., Marín, M., Navarro, S., Torres, J., Vasavada, A., 2016. The meteorology of Gale Crater as determined from Rover Environmental Monitoring Station observations and numerical modeling. Part II: Interpretation. *Icarus* 280, 114–138.
- Rafkin, S. C. R., Sta. Maria, M. R. V., Michaels, T. I., 2002. Simulation of the atmospheric thermal circulation of a martian volcano using a mesoscale numerical model. *Nature* 419, 697–699.

- Ramirez, R. M., 2017. A warmer and wetter solution for early Mars and the challenges with transient warming. *Icarus* 297, 71–82.
- Reiss, D., Fenton, L., Neakrase, L., Zimmerman, M., Statella, T., Whelley, P., Rossi, A. P., Balme, M., 2016. Dust Devil Tracks. *Space Sci. Rev.* 203, 143–181.
- Renfrew, I. A., Anderson, P. S., 2006. Profiles of katabatic flow in summer and winter over Coats Land, Antarctica. *Q. J. R. Meteorol. Soc.* 132, 779–802.
- Robbins, S. J., Hynes, B. M., 2012. A new global database of Mars impact craters  $\geq 1$  km: 2. Global crater properties and regional variations of the simple-to-complex transition diameter. *J. Geophys. Res. (Planets)* 117, E06001.
- Salese, F., Ansan, V., Mangold, N., Carter, J., Ody, A., Poulet, F., Ori, G. G., 2016. A sedimentary origin for intercrater plains north of the Hellas basin: Implications for climate conditions and erosion rates on early Mars. *J. Geophys. Res. (Planets)* 121, 2239–2267.
- Savijarvi, H., Siili, T., 1993. The Martian slope winds and the nocturnal PBL jet. *J. Atmos. Sci.* 50, 77–88.
- Shao, Y., 2008. *Physics and Modelling of Wind Erosion*.
- Shapiro, A., Fedorovich, E., Rahimi, S., 2016. A Unified Theory for the Great Plains Nocturnal Low-Level Jet. *J. Atmos. Sci.* 73, 3037–3057.
- Silvestro, S., Fenton, L. K., Vaz, D. A., Bridges, N. T., Ori, G. G., 2010. Ripple migration and dune activity on Mars: Evidence for dynamic wind processes. *Geophys. Res. Lett.* 37, L20203.
- Silvestro, S., Vaz, D. A., Ewing, R. C., Rossi, A. P., Fenton, L. K., Michaels, T. I., Flahaut, J., Geissler, P. E., 2013. Pervasive aeolian activity along rover Curiosity’s traverse in Gale Crater, Mars. *Geology* 41, 483–486.
- Smith, D. E., Zuber, M. T., Frey, H. V., Garvin, J. B., Head, J. W., Muhleman, D. O., Pettengill, G. H., Phillips, R. J., Solomon, S. C., Zwally, H. J., Banerdt, W. B., Duxbury, T. C., Golombek, M. P., Lemoine, F. G., Neumann, G. A., Rowlands, D. D., Aharonson, O., Ford, P. G., Ivanov, A. B., Johnson, C. L., McGovern, P. J., Abshire, J. B., Afzal, R. S., Sun, X., 2001. Mars Orbiter Laser Altimeter: Experiment summary after the first year of global mapping of Mars. *J. Geophys. Res.* 106, 23689–23722.
- Soto, A., Mischna, M., Schneider, T., Lee, C., Richardson, M., 2015. Martian atmospheric collapse: Idealized GCM studies. *Icarus* 250, 553–569.
- Spiga, A., 2011. Elements of comparison between Martian and terrestrial mesoscale meteorological phenomena: Katabatic winds and boundary layer convection. *Planet. Space Sci.* 59, 915–922.

- Spiga, A., Forget, F., 2009. A new model to simulate the Martian mesoscale and microscale atmospheric circulation: Validation and first results. *J. Geophys. Res. (Planets)* 114, E02009.
- Spiga, A., Forget, F., Madeleine, J.-B., Montabone, L., Lewis, S. R., Millour, E., 2011. The impact of martian mesoscale winds on surface temperature and on the determination of thermal inertia. *Icarus* 212, 504–519.
- Squyres, S. W., Arvidson, R. E., Bell, J. F., Calef, F., Clark, B. C., Cohen, B. A., Crumpler, L. A., de Souza, P. A., Farrand, W. H., Gellert, R., Grant, J., Herkenhoff, K. E., Hurowitz, J. A., Johnson, J. R., Jolliff, B. L., Knoll, A. H., Li, R., McLennan, S. M., Ming, D. W., Mittlefehldt, D. W., Parker, T. J., Paulsen, G., Rice, M. S., Ruff, S. W., Schröder, C., Yen, A. S., Zacny, K., 2012. Ancient Impact and Aqueous Processes at Endeavour Crater, Mars. *Science* 336, 570.
- Steakley, K., Murphy, J., 2016. A year of convective vortex activity at Gale crater. *Icarus* 278, 180–193.
- Steele, L. J., Balme, M. R., Lewis, S. R., Spiga, A., 2017. The water cycle and regolith-atmosphere interaction at Gale crater, Mars. *Icarus* 289, 56–79.
- Sullivan, R., Kok, J. F., 2017. Aeolian Saltation on Mars at Low Wind Speeds. Accepted for publication in *J. Geophys. Res. (Planets)*.
- Tanaka, K. L., 2000. Dust and Ice Deposition in the Martian Geologic Record. *Icarus* 144, 254–266.
- Thomson, B. J., Bridges, N. T., Milliken, R., Baldrige, A., Hook, S. J., Crowley, J. K., Marion, G. M., de Souza Filho, C. R., Brown, A. J., Weitz, C. M., 2011. Constraints on the origin and evolution of the layered mound in Gale Crater, Mars using Mars Reconnaissance Orbiter data. *Icarus* 214, 413–432.
- Tornabene, L. L., Osinski, G. R., McEwen, A. S., Ling, V., Caudill, C. M., Nuhn, A., Hopkins, R., D’Aoust, B., Kasmai, B., Mattson, S. 2014. A Global Synthesis of the Meter- to Decameter-Scale Morphology and Structure of Complex Crater Central Uplifts. In *Eighth International Conference on Mars*, volume 1791 of LPI Contributions, page 1379.
- Tornabene, L. L., Watters, W. A., Osinski, G. R., Boyce, J. M., Harrison, T. N., Ling, V., McEwen, A. S., 2018. A depth versus diameter scaling relationship for the best-preserved melt-bearing complex craters on Mars. *Icarus* 299, 68–83.
- Tyler, D., Barnes, J. R., 2015. Convergent crater circulations on Mars: Influence on the surface pressure cycle and the depth of the convective boundary layer. *Geophys. Res. Lett.* 42, 7343–7350.

- Tyler, D., Barnes, J. R., Haberle, R. M., 2002. Simulation of surface meteorology at the Pathfinder and VL1 sites using a Mars mesoscale model. *J. Geophys. Res. (Planets)* 107, 2–1.
- Tyler, Jr., D., Barnes, J. R., 2013. Mesoscale Modeling of the Circulation in the Gale Crater Region: An Investigation into the Complex Forcing of Convective Boundary Layer Depths. *Mars* 8, 58–77.
- Villagrasa, D. M., Lehner, M., Whiteman, C. D., Hoch, S. W., Cuxart, J., 2013. The Upslope-Downslope Flow Transition on a Basin Sidewall. *J. Appl. Meteor. Climatol.* 52, 2715–2734.
- Wang, P., Zheng, X., 2015. Unsteady saltation on Mars. *Icarus* 260, 161–166.
- Wang, Z.-T., Wang, H.-T., Niu, Q.-H., Dong, Z.-B., Wang, T., 2011. Abrasion of yardangs. *Phys. Rev. E* 84 (3), 031304.
- White, B. R., 1979. Soil transport by winds on Mars. *J. Geophys. Res.* 84, 4643–4651.
- Whiteman, C. D., Hoch, S. W., Lehner, M., Haiden, T., 2010. Nocturnal Cold-Air Intrusions into a Closed Basin: Observational Evidence and Conceptual Model. *J. Appl. Meteor. Climatol.* 49, 1894–1905.
- Wordsworth, R. D., 2016. The Climate of Early Mars. *Annu. Rev. Earth Planet. Sci.* 44, 381–408.
- Ye, Z. J., Segal, M., Pielke, R. A., 1990. A comparative study of daytime thermally induced upslope flow on Mars and earth. *J. Atmos. Sci.* 47, 612–628.
- Zabrusky, K., Andrews-Hanna, J. C., Wiseman, S. M., 2012. Reconstructing the distribution and depositional history of the sedimentary deposits of Arabia Terra, Mars. *Icarus* 220, 311–330.